AIAA JOURNAL
Vol. 30, No. 11, November 1992

RIPPLE: A New Model for Incompressible Flows with Free Surfaces

D. B. Kothe* and R. C. Mjolsness*
Los Alamos National Laboratory, Los Alamos, New Mexico 87545

A new free-surface flow model, RIPPLE, is summarized. RIPPLE obtains finite difference solutions for incompressible flow problems having significant surface tension forces at free surfaces of arbitrarily complex topology. The key innovation is the continuum surface force model, which represents surface tension as a localized volume force. Other features include a higher order momentum advection model, a volume-of-fluid free-surface treatment, and an efficient two-step projection solution method. RIPPLE's unique capabilities are illustrated with two example problems: low-gravity jet-induced tank flow, and the collision and coalescence of two cylindrical rods.

Introduction

RIPPLE models transient, two-dimensional, incompressible fluid flows with surface tension on free surfaces of general topology.[1] Finite difference solutions to the incompressible Navier-Stokes equations are obtained on an Eulerian, rectilinear mesh in Cartesian or cylindrical geometries. Free surfaces are represented with volume-of-fluid (VOF) data on the mesh. Surface tension is modeled as a volume force derived from the continuum surface force (CSF) model.[2] A two-step projection method is used for the incompressible fluid flow solutions, aided by an incomplete Cholesky conjugate gradient (ICCG) solution technique[3] for the pressure Poisson equation (PPE). Momentum advection is estimated with the weakly monotonic, second-order upwind method of van Leer.[1] Flow obstacles and curved boundaries interior to the mesh are represented with a partial cell treatment.

The RIPPLE numerical scheme contains modern algorithms that reflect recent improvements and advances,[2-4] resulting in increased robustness and accuracy relative to solution algorithm (SOLA)-VOF algorithms for incompressible flow.[5-7] Because the VOF technique is both a practical and accurate Eulerian free-surface model, we have retained the VOF representation of fluid interfaces[8] as the one common element between RIPPLE and SOLA-VOF models.

RIPPLE is a versatile tool capable of modeling a wide range of applications, being especially suited for low Bond number, low Weber number, and low capillary number flows in which fluid accelerations are weak and fluid restoring forces (e.g., surface tensions) are strong. A brief summary of the physical model and numerical algorithms comprising RIPPLE is given. Its properties are then illustrated by two example calculations.

Physical Model

In the following, we briefly discuss the RIPPLE models for incompressible hydrodynamics, free surfaces, surface tension, wall adhesion, and flow obstacles.

Hydrodynamics

The governing equations are the incompressibility condition,

$$\nabla \cdot V = 0 \tag{1}$$

and the transport of fluid momentum,

$$\frac{\partial V}{\partial t} + \nabla \cdot (VV) = -\frac{1}{\rho}\nabla p + \frac{1}{\rho}\nabla \cdot \tau + g + \frac{1}{\rho}F_b \tag{2}$$

where V is the fluid velocity, ρ the density, p the scalar pressure, τ the viscous stress tensor, F_b a body force, and g the acceleration due to gravity. The nonlinear advection term is written in conservative form. The viscous stress tensor τ is Newtonian,

$$\tau = 2\mu S, \qquad S = \tfrac{1}{2}[(\nabla V) + (\nabla V)^T] \tag{3}$$

where S is the rate-of-strain tensor and μ the coefficient of dynamic viscosity.

Free Surfaces

To avoid the topological restrictions associated with modeling free surfaces with logically connected Lagrangian points, as in the Lagrangian incompressible (LINC) technique,[9] or with logically connected massless particles, as in the marker and cell (MAC) technique with surface tension,[10,11] free surfaces are represented in RIPPLE with discrete VOF data on the mesh. The VOF method, pioneered by Nichols et al.[5] and Hirt and Nichols,[8] is a powerful tool that enables a finite difference representation of free surfaces and interfaces that are arbitrarily oriented with respect to the computational grid.[12] It has been used with success in both Eulerian and arbitrary Lagrangian-Eulerian (ALE) schemes.[4] In the VOF technique, an exact representation of the free surface is not retained. Characteristic marker data (i.e., the VOF function F), advected as a Lagrangian invariant, is propagated according to

$$\frac{dF}{dt} = \frac{\partial F}{\partial t} + (V \cdot \nabla)F = 0 \tag{4}$$

where $F(x, 0)$ is given by initializing the free surface geometry. In RIPPLE, F is equal to 1 in the fluid, 0 in the void, and $0 \le F \le 1$ at the free surface. Since F is the only available free-surface information, an approximate reconstruction of the free surface must be performed to obtain the free-surface location.

Sharp interfaces are maintained by insuring sharp gradients in F. This results numerically from a special treatment of the advective term in Eq. (4), which models the movement of the fluid through the mesh. A standard treatment of this term (i.e., a centered difference or donor cell approximation) leads to an unacceptable amount of numerical diffusion and spreading of the free-surface region. An approximate free-surface

Presented as Paper 91-3548 at the AIAA/NASA/OAI Conference on Advanced SEI Technologies, Cleveland, OH, Sept. 4-6, 1991; received Sept. 17, 1991; revision received April 27, 1992; accepted for publication April 27, 1992.

*Staff Member, Fluid Dynamics Group T-3, Theoretical Division, Mail Stop B216.

reconstruction is the crucial step necessary for computing accurate flux volumes needed for the advective term. The reconstructed free surface is not normally continuous, instead it is represented as a set of discrete, discontinuous line segments.

Surface Tension

Surface tension at free surfaces is modeled in RIPPLE with a localized volume force prescribed by the CSF model.[2] Ideally suited for Eulerian interfaces of arbitrary topology, the CSF model's volume reformulation is a new and radical departure from conventional finite difference representations of surface tension. We discuss the CSF model briefly here and refer the interested reader to Ref. 2 for further details on theory and numerical implementation.

In RIPPLE, viscous effects are neglected at the free surface and the surface tension coefficient σ is assumed to be constant, implying that the surface force has no tangential component. Thus, the stress boundary condition reduces to Laplace's formula,[13]

$$p_s \equiv p - p_v = \sigma\kappa \tag{5}$$

where the surface pressure p_s is the surface tension-induced pressure jump, p_v the vapor pressure, and κ the mean free-surface curvature, given by[2]

$$\kappa = -(\nabla \cdot \hat{n}) = \frac{1}{|n|}\left[\left(\frac{n}{|n|}\cdot\nabla\right)|n| - (\nabla \cdot n)\right] \tag{6}$$

where the unit normal $\hat{n}$,

$$\hat{n} = \frac{n}{|n|} \tag{7}$$

is derived from a normal vector n,

$$n = \nabla F \tag{8}$$

that is the gradient of VOF data. Because the curvature is proportional to the second derivatives of the VOF function, surface force modeling is extraordinarily sensitive to small errors in F. The CSF model results in a more regular evolution of fluid surfaces.[1,2]

In the CSF model, surface tension is reformulated as a volume force F_{sv} satisfying

$$\lim_{h\to 0}\int_{\Delta V} F_{sv}(x)d^3x = \int_{\Delta S} F_{sa}(x_s)\, dS \tag{9}$$

where x_s is a point on the surface, $F_{sa}(x)$ the surface tension force per unit interfacial area,

$$F_{sa}(x_s) = \sigma\kappa(x_s)\hat{n}(x_s) \tag{10}$$

and h is a length comparable to the resolution afforded by a computational mesh with spacing δx. The area integral is over the portion ΔS of the surface lying within the small volume of integration ΔV. The finite difference approximations in RIPPLE replace free-surface discontinuities with finite thickness transition regions within which the fluid properties, or "color," vary smoothly from fluid to vapor over a distance of $\mathcal{O}(h)$. The volume force, nonzero only within free surfaces, is given in the CSF model by[2]

$$F_{sv}(x) = \sigma\kappa(x)\frac{\nabla\tilde{c}(x)}{[c]} \tag{11}$$

where $\tilde{c}$ is the fluid color, equated with the VOF function F in RIPPLE, and $[c]$ is the jump in color, equal to 1.0 when $\tilde{c} = F$. The color function, which serves as a unique material identifier, is here most simply taken to be the VOF function. When $\tilde{c} = F$, the volume force is computed accurately for any two fluids meeting at the interface. In particular, the two fluids could have equal densities.

With the volume force F_{sv}, surface tension effects at free surfaces are modeled as a body force in the momentum transport equation [Eq. (2)]:

$$F_b = F_{sv} \tag{12}$$

The volume force F_{sv} is of course in addition to other arbitrary body forces present in the flow.

Instead of a surface tensile force or a surface pressure boundary condition applied at a discontinuity, a volume force F_{sv} in Eq. (11) acts on fluid elements lying within finite thickness transition regions replacing the discontinuities. It is not appropriate, therefore, to apply in finite difference schemes a pressure jump induced by surface tension at a free surface discontinuity. In this model, surface tension acts everywhere within the transition region through the volume force F_{sv}.

Wall Adhesion

Wall adhesion is the surface force acting on fluid interfaces at points of contact with walls, which are static, rigid boundaries in RIPPLE. Wall adhesion forces are calculated in the same manner as volume forces due to surface tension are calculated, using Eq. (11) for F_{sv}, except that a boundary condition is applied to the free surface unit normal $\hat{n}$ prior to evaluating Eq. (11). The condition is applied only to those vertex normals lying on or near a rigid boundary, which is either an interior obstacle boundary or a mesh boundary. Those forces F_{sv} attributed to wall adhesion are therefore only in cells within proximity of a wall.

The wall adhesion boundary condition becomes an expression for the unit free surface normal $\hat{n}$ at points of contact x_w along the wall:

$$\hat{n} = \hat{n}_w \cos\theta_{eq} + \hat{t}_w \sin\theta_{eq} \tag{13}$$

where θ_{eq} is the static contact angle between the fluid and the wall, $\hat{n}_w$ the unit wall normal directed into the wall, and $\hat{t}_w$ the tangent to the wall, normal to the contact line between the free surface and the wall at x_w. The equation uses the geometric identity that θ_{eq}, defined as the angle between the tangent to the fluid and $\hat{t}_w$, is also the angle between $\hat{n}_w$ and $\hat{n}$. The unit tangent $\hat{t}_w$ is directed into the fluid and is computed from Eq. (8) with the VOF function F reflected at the wall. The angle θ_{eq} is not a fluid material property, but a system property, depending also on properties of the wall itself. The value of θ_{eq} is measured experimentally when the fluid is at rest. We emphasize that Eq. (13) is applied at a wall whether or not VOF data indicates that the fluid is actually making an angle of contact equal to θ_{eq}.

The RIPPLE treatment of wall adhesion is both a physical and a numerical approximation. It is a physical approximation because θ_{eq} is assumed to be a constant when in reality it depends on the local wall and fluid conditions (i.e., velocity, viscosity, and surface tensions). The numerical approximation results from an inexact treatment of the wall geometries. Both approximations, however, do not prevent the wall adhesion forces in RIPPLE from being qualitatively correct.

The physical approximation in wall adhesion stems from using the static angle θ_{eq} rather than the moving contact angle θ_M more appropriate to a moving contact line. Unless RIPPLE were applied to a very localized study of a moving contact line, it would not have the resolution capability to make use of the actual moving contact angle, which cannot currently be measured. The angle θ_M depends in a complex way on material and fluid dynamic properties, being at the very least a function of θ_{eq} and the capillary number $Ca = V\mu/\sigma$. For many materials, the dependence has not been well characterized. The present algorithm should be adequate when the difference between θ_M and θ_{eq} is not very large, and so RIPPLE's wall adhesion treatment is likely to be a good approximation when θ_{eq} is small.

Flow Obstacles

Obstacles to flow are modeled in RIPPLE as a special case of two-phase flow, in which the first phase is the fluid, with volume fraction Θ, and the second "phase" is the obstacle, with volume fraction $1.0 - \Theta$. The obstacle is characterized as a "fluid" of infinite density and zero velocity. Since all calculations are performed in the obstacle frame, obstacles are static, and so the volume fraction Θ is a time-independent scalar field $\Theta = \Theta(\boldsymbol{x})$ that is a step function:

$$\Theta(\boldsymbol{x}) = \begin{cases} 1.0, & \text{in the fluid} \\ 0.0, & \text{in the obstacle} \end{cases} \tag{14}$$

The volume fraction Θ, referred to as a partial flow flag, is a perfect step function only when obstacle boundaries coincide with mesh lines representing lines of constant x and y. In general, however, obstacle boundaries snake arbitrarily through the mesh, cutting through cells. This gives rise to a continuous range of Θ from 0.0 to 1.0, which is necessary to avoid a stair-step model of a curved interior obstacle boundary. Those cells having a value of Θ satisfying $0 < \Theta < 1$ are termed partial flow cells because a portion Θ of their finite difference volume is open to flow and the remaining portion $1.0 - \Theta$ is occupied by an obstacle closed to flow.

Numerical Model

Finite difference conventions follow that of the MAC scheme,[10] in which x- and y-velocity components are located at cell face centers on lines of constant x and y, respectively, and the pressure and VOF function are located at cell centers. From Fig. 1, the pressure $p_{i,j}$ and VOF function $F_{i,j}$ are located at $\boldsymbol{x}_{i,j} = (x_{i-\frac{1}{2}} + \delta x_i/2)\hat{i} + (y_{j-\frac{1}{2}} + \delta y_j/2)\hat{j}$. The x velocity $u_{i+\frac{1}{2},j}$ resides at $\boldsymbol{x}_{i+\frac{1}{2},j}$ and the y velocity $v_{i,j+\frac{1}{2}}$ resides at $\boldsymbol{x}_{i,j+\frac{1}{2}}$.

Equations (1) and (2) are solved in finite difference form with a two-step projection method involving the time discretization of the momentum equation, namely

$$\frac{\tilde{\boldsymbol{V}} - \boldsymbol{V}^n}{\delta t} = -\nabla\cdot(\boldsymbol{V}\boldsymbol{V})^n + \frac{1}{\rho^n}\nabla\cdot\tau^n + \boldsymbol{g}^n + \frac{1}{\rho^n}\boldsymbol{F}_b^n \tag{15}$$

$$\frac{\boldsymbol{V}^{n+1} - \tilde{\boldsymbol{V}}}{\delta t} = -\frac{1}{\rho^n}\nabla p^{n+1} \tag{16}$$

$$\nabla\cdot\boldsymbol{V}^{n+1} = 0 \tag{17}$$

In the first step, a velocity field $\tilde{\boldsymbol{V}}$ is computed from incremental changes in the field $\boldsymbol{V}^n$ resulting from viscosity, advection, gravitational accelerations, and body forces. In the second step, this velocity field is projected onto a zero-divergence vector field. The two equations in the second step can be combined into a single Poisson equation for the pressure,

$$\nabla\cdot\left[\frac{1}{\rho^n}\nabla p^{n+1}\right] = \frac{\nabla\cdot\tilde{\boldsymbol{V}}}{\delta t} \tag{18}$$

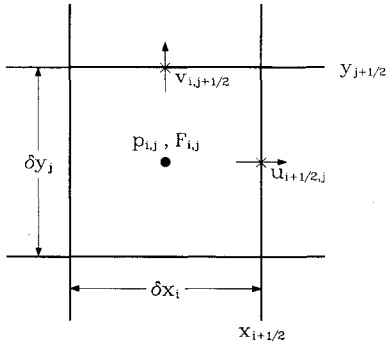

Fig. 1 Location of fluid variables in a RIPPLE computational cell. The x and y velocities are located at cell faces, and the pressure $p_{i,j}$ and VOF function $F_{i,j}$ are located at cell centers.

which will be referred to as the PPE. Although the incompressible solutions in RIPPLE are for constant density fluids, the density in Eq. (18) is retained inside the divergence operator. This results in an extra term in the PPE proportional to $\nabla\rho$, which contributes to the pressure solution within the free-surface transition region where $\nabla\rho \neq 0$. The PPE is formulated with the pressure p and density ρ as separate terms, instead of using a single term, the kinematic pressure, p/ρ, as in the majority of incompressible models.

Momentum Advection

A finite volume approximation of conservative momentum advection results from integrating the advection term in Eq. (15) over the control volume V_{cv}, giving

$$\int_{V_{cv}} \nabla\cdot(\boldsymbol{V}\boldsymbol{V})\,\mathrm{d}V = \sum_s \langle\boldsymbol{V}\rangle_s(\boldsymbol{V}_s\cdot\hat{\boldsymbol{n}}_s)\delta\boldsymbol{A}_s\cdot\hat{\boldsymbol{n}}_s \tag{19}$$

where Gauss' theorem has been used and the area integral has been expressed in discrete form as a sum over sides s surrounding the control volume. At each side, the velocity is $\boldsymbol{V}_s$, the unit outward normal is $\hat{\boldsymbol{n}}_s$, and the area is $\delta A_s = \delta\boldsymbol{A}_s\cdot\hat{\boldsymbol{n}}_s$. The flux velocity is $\boldsymbol{V}_s\cdot\hat{\boldsymbol{n}}_s$, and so the flux volume is $(\boldsymbol{V}_s\cdot\hat{\boldsymbol{n}}_s)\delta A_s\delta t_{\mathrm{adv}}$, where δt_{adv} is the advection time step. The bracketed term $\langle\boldsymbol{V}\rangle_s$ is the quantity to be fluxed, which is the velocity for constant density momentum advection.

The summation term in Eq. (19) becomes, e.g.,

$$[r_{i+1}^{\delta}\langle u\rangle_R u_{\mathrm{fl}i+1,j} - r_i^{\delta}\langle u\rangle_L u_{\mathrm{fl}i,j}]\delta y_j + [\langle u\rangle_T v_{\mathrm{fl}i+\frac{1}{2},j+\frac{1}{2}} - \langle u\rangle_B v_{\mathrm{fl}i+\frac{1}{2},j-\frac{1}{2}}]\delta x_{i+\frac{1}{2}}$$

for integration over the x-momentum control volume. The superscript δ on the radius r is a constant equal to 1 in cylindrical and 0 in Cartesian geometry. The bracketed terms, i.e., $\langle u\rangle_R$, are estimated with either an interpolated donor cell, a centered difference, or an upstream, second-order van Leer approximation.[1] The van Leer algorithm gives the best results in practice because it attempts to preserve monotonicity of the fluxed quantities within a second-order scheme.

An advection finite difference operator $\mathcal{L}_k$ can be defined for component k in Eq. (19):

$$\mathcal{L}_k(\boldsymbol{V}) = \frac{\delta t_{\mathrm{adv}}}{V_{\mathrm{cv}k}}\sum_s \langle\boldsymbol{V}\rangle_s(\boldsymbol{V}_s\cdot\hat{\boldsymbol{n}}_{sk})\delta\boldsymbol{A}_s\cdot\hat{\boldsymbol{n}}_{sk} \tag{20}$$

where $V_{\mathrm{cv}k}$ is $V_{\mathrm{cv}x} = r_{i+\frac{1}{2}}^{\delta}\delta x_{i+\frac{1}{2}}\delta y_j$ for x momentum and $V_{\mathrm{cv}y} = r_i^{\delta}\delta x_i\delta y_{j+\frac{1}{2}}$ for y momentum. With this operator, the RIPPLE finite difference form of the advection term of Eq. (15) can be rewritten as

$$\boldsymbol{V}^{n+1} = \boldsymbol{V}^n - \mathcal{L}_x\mathcal{L}_y\mathcal{L}_y\mathcal{L}_x(\boldsymbol{V}^n) \tag{21}$$

Advection is therefore broken down into four separate one-dimensional sweeps, ordered x-y-y-x, each with an advection time step δt_{adv} that is one-half of the time step δt used in differencing Eq. (15). The subcycled, directionally split operator gives a more accurate approximation to advective momentum transport in directions misaligned with the coordinate axes. It also adds back some $\mathcal{O}(\delta t^2)$ contributions that are lost in a first-order, forward time difference of Eq. (15).

Pressure Poisson Equation Solution

A finite difference approximation to Eq. (18) leads to a system of linear equations. The resulting matrix equation is solved with an ICCG solution technique[3] that returns the time t^{n+1} pressure in every cell, regardless of whether that cell represents fluid, surface, void, or an obstacle. Special attention must therefore be paid to cell face values of the ratio of a geometric coefficient to the fluid density (i.e., α/ρ) in cells within an obstacle, a void, or the free surface. This ratio is expressed within the free surface as a quotient of two averages

rather than an average of two quotients, thereby keeping the principal contribution within the free-surface region rather than at the edge near the void.[1]

We obtain a matrix M that is symmetric and positive definite in addition to being sparse and banded, thus inverted easily and quickly with ICCG methods.[3] The ICCG method is a hybrid matrix scheme that combines an incomplete Cholesky decomposition preconditioning of M with a conjugate gradient iteration. The decomposition transforms M into LDL^T+E, where L is a lower triangular matrix, D is a diagonal matrix (an approximate identity matrix), and E is a small error matrix. A conjugate gradient algorithm then accelerates an equivalent problem, neglecting E, toward the solution x of $L^{-1}M(L^T)^{-1}(L^Tx)=L^{-1}y$, where $(LL^T)^{-1}$ is used as an approximate inverse for M. With the ICCG method, most solutions requiring $\epsilon=\nabla\cdot V=10^{-8}$ converge in less than 25 iterations, regardless of the magnitude of the source term (right-hand sides of Eq. 18).

Volume-of-Fluid Advection

A numerical solution of Eq. (4) requires flux volumes for the advective term. The flux volumes are obtained in RIPPLE with a free surface reconstruction using the Hirt-Nichols (H-N) algorithm.[8] The free surface is reconstructed either horizontally or vertically in each surface cell, depending on its relation to neighboring cells. This reconstruction is presumably more accurate than the simple line interface calculation (SLIC) algorithm,[14] where the reconstructed free surface is always forced perpendicular to the fluxing direction, but less accurate than the Youngs algorithm,[15] where the reconstructed free surface is allowed to have nonzero slope.

The numerical solution of Eq. (4) is initiated by defining a tilde value of F,

$$\tilde{F}=F^n-\delta t\,\nabla\cdot(VF^n) \tag{22}$$

It is completed with a divergence correction,

$$F^{n+1}=\tilde{F}+\delta t(\nabla\cdot V)F^n \tag{23}$$

bringing $\tilde{F}$ to F^{n+1}.

Equation (22) is discretized by integrating over the mass control volume, whose boundaries are the cell boundaries, giving

$$\tilde{F}_{i,j}=F^n_{i,j}-\frac{\delta t}{r_i^{\delta}\delta x_i}\left[r^{\delta}_{i+\frac{1}{2}}u^{n+1}_{i+\frac{1}{2},j}\langle F\rangle_R-r^{\delta}_{i-\frac{1}{2}}u^{n+1}_{i-\frac{1}{2},j}\langle F\rangle_L\right]$$
$$-\frac{\delta t}{\delta y_j}\left[v^{n+1}_{i,j+\frac{1}{2}}\langle F\rangle_T-v^{n+1}_{i,j-\frac{1}{2}}\langle F\rangle_B\right] \tag{24}$$

where subscripts B, T, L, and R denote quantities taken at the bottom, top, left, and right sides, respectively, of cell (i,j). VOF advection is computed at the end of each computational cycle, completing the second step of the projection method,

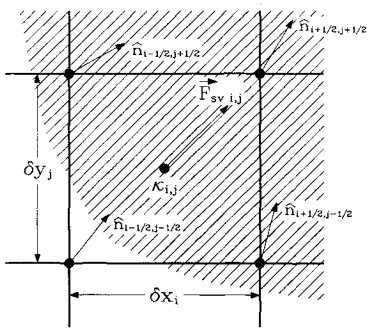

Fig. 2 In the CSF model for surface tension, a cell-centered volume force due to surface tension F_{sv} is derived from a free-surface curvature κ at the cell center and unit normals $\hat{n}$ at the four cell vertices.

and so the velocities advecting F in Eq. (24) are those at the time t^{n+1}. Bracketed quantities are the fractional fluid volumes crossing each cell boundary. It is these quantities that are estimated with a free-surface reconstruction. Given, as an example, are the RIPPLE expressions for $\langle F\rangle_R$ when $u^{n+1}_{i-\frac{1}{2},j}>0$. Calculation of $\langle F\rangle$ values follow directly from the H-N reconstruction algorithm, as stated previously.

The VOF function fluxed at the right face of cell (i,j) is the sum of an upstream value $F_{iad,j}$ plus an increment δF:

$$\langle F\rangle_R=F_{iad,j}+\delta F \tag{25}$$

where the VOF increment,

$$\delta F=0,\quad \text{if}\quad w=0.0\quad\text{or}\quad w>\left|u^{n+1}_{i+\frac{1}{2},j}\delta t\right| \tag{26}$$

$$\delta F=(F_{idm,j}-F_{ia,j})\left(1-w\left|u^{n+1}_{i+\frac{1}{2},j}\delta t\right|^{-1}\right)$$
$$\text{if}\quad 0.0<w<\left|u^{n+1}_{i+\frac{1}{2},j}\delta t\right| \tag{27}$$

depends on the relative value of a void width w, defined nonzero only when the reconstructed surface is parallel to the fluxing direction, given by

$$w=\left(\frac{F_{idm,j}-F_{id,j}}{F_{idm,j}-F_{ia,j}}\right)\delta x_i \tag{28}$$

The donor *id*, acceptor *ia*, and donor-minus *idm* cell indices are always i, $i+1$, and $i-1$, respectively. The quantity $F_{iad,j}$ is not necessarily the upstream VOF, as can seen by case analysis.[1] Similar free surface reconstructions are performed for estimates of flux quantities $\langle F\rangle_L$, $\langle F\rangle_T$, and $\langle F\rangle_B$.

Continuum Surface Force Model

Surface tension modeled with the CSF model eliminates the need for detailed interface information, and so restrictions on the number, complexity, or dynamic evolution of interfaces having surface tension are not imposed. Direct comparisons between modeling surface tension with the CSF model in RIPPLE and with a popular interface reconstruction model[6,7] show that the CSF model makes more accurate use of the free-surface VOF data.[2] The volume force always tends to force the free-surface to seek a minimum surface energy configuration. Reconstruction models, on the other hand, tend to induce numerical noise from computed graininess in the surface pressures, often leading to unphysical free surface disruptions. In addition to providing a more accurate finite difference representation of surface tension without the topological restrictions, the CSF model is easy to implement computationally. Surface tension is easily included by calculating and applying an extra body force F_{sv} in the momentum equation. In the majority of RIPPLE calculations, only a few percent of extra CPU time is required for computing surface tension effects.

The volume force in the CSF model is easily calculated by taking first- and second-order spatial derivatives of the VOF function F. At each point within the free surface transition region, a cell-centered value F_{sv} is defined, which is proportional to the cell-centered curvature κ of the constant VOF surface at that point. The curvature is obtained from vertex-centered normal vectors, as illustrated in Fig. 2. The force is normalized to recover the conventional description of surface tension as the local product $\kappa h\to 0$. Its line integral directed normally through the free-surface transition region is approximately equal to the surface pressure in Eq. (5).

From Eq. (8), n at vertex $(i+\frac{1}{2},j+\frac{1}{2})$ is given by

$$\frac{(F_{i+1,j+1}-F_{i,j+1})\delta y_j+(F_{i+1,j}-F_{i,j})\delta y_{j+1}}{(\delta y_j+\delta y_{j+1})\delta x_{i+\frac{1}{2}}}$$

for the x component n_x, and

$$\frac{(F_{i+1,j+1} - F_{i+1,j})\delta x_i + (F_{i,j+1} - F_{i,j})\delta x_{i+1}}{(\delta x_i + \delta x_{i+1})\delta y_{j+\frac{1}{2}}}$$

for the y component n_y. The curvature follows from an indirect differentiation of the unit normal $\hat{n}$, as given by the two terms on the right-hand side of Eq. (6). The derivatives of the components of $\boldsymbol{n}$ follow easily from knowledge of $\boldsymbol{n}$ at vertices. Representatives values are given by

$$\left(\frac{\partial n_x}{\partial x}\right)_{i,j} = \frac{1}{2\delta x_i}\left[n_{xi+\frac{1}{2},j+\frac{1}{2}} + n_{xi+\frac{1}{2},j-\frac{1}{2}} - n_{xi-\frac{1}{2},j+\frac{1}{2}} - n_{xi-\frac{1}{2},j-\frac{1}{2}}\right] \quad (29)$$

$$\left(\frac{\partial n_x}{\partial y}\right)_{i,j} = \frac{1}{2\delta y_j}\left[n_{xi+\frac{1}{2},j+\frac{1}{2}} + n_{xi-\frac{1}{2},j+\frac{1}{2}} - n_{xi+\frac{1}{2},j-\frac{1}{2}} - n_{xi-\frac{1}{2},j-\frac{1}{2}}\right] \quad (30)$$

The cell-centered normal is the average of vertex normals,

$$\boldsymbol{n}_{i,j} = \tfrac{1}{4}(\boldsymbol{n}_{i+\frac{1}{2},j+\frac{1}{2}} + \boldsymbol{n}_{i+\frac{1}{2},j-\frac{1}{2}} + \boldsymbol{n}_{i-\frac{1}{2},j+\frac{1}{2}} + \boldsymbol{n}_{i-\frac{1}{2},j-\frac{1}{2}}) \quad (31)$$

Face-centered values of $\boldsymbol{F}_{sv}$ are needed for the computation of fluid acceleration due to surface tension in RIPPLE and are obtained by interpolating from the two nearest cell-centered values, giving

$$F_{svxi+\frac{1}{2},j} = \frac{\delta x_i F_{svxi+1,j} + \delta x_{i+1} F_{svxi,j}}{\delta x_i + \delta x_{i+1}} \quad (32)$$

for the x component at the right face of cell (i,j), and

$$F_{svyi,j+\frac{1}{2}} = \frac{\delta y_j F_{svyi,j+1} + \delta y_{j+1} F_{svyi,j}}{\delta y_j + \delta y_{j+1}} \quad (33)$$

for the y component at the top face. The face-centered components of $\boldsymbol{F}_{sv}$ are then used to compute fluid accelerations from

$$\rho \frac{\partial \boldsymbol{V}}{\partial t} = \boldsymbol{F}_{sv} \quad (34)$$

completing the first step of the two-step projection method.

When the surface tension coefficient σ is variable, e.g., due to the presence of surfactants or temperature gradients, the resulting tangential component of the surface force may be modeled within the framework of the CSF model. The model may also be extended to three dimensions and to multifluid flows.

Wall Adhesion

The wall adhesion boundary condition is enforced by computing the normal at wall vertices from Eq. (13). While this procedure introduces finite-difference errors in general, it produces a qualitatively correct restoring force.

The wall adhesion boundary condition in Eq. (13) is applied only to unit free-surface normals residing at vertices, and so the wall boundary is in effect forced always to coincide with cell boundaries. This is, of course, an error for those cells containing a rigid, interior obstacle boundary that does not coincide with a grid line. An example is in Fig. 3, where a wall boundary cuts through the interior of a cell as shown. In this case, $\sqrt{2}/2 < \hat{n}_w \cdot \hat{\imath} < 1$, so the wall is assumed to be a right wall; hence, the equation is applied only to the two $i + \frac{1}{2}$ vertex normals. Similar considerations apply for left walls (the two $i - \frac{1}{2}$ vertices), top walls (the two $j + \frac{1}{2}$ vertices), and bottom walls (the two $j - \frac{1}{2}$ vertices). The result of Eq. (13) in Fig. 3 is to force the surface normal $\hat{n}$ to take on the value it would have in static contact with the wall (with the geometry displayed in Fig. 3) rather than the value that would be calculated from VOF data. This gives rise to a strong local volume force $\boldsymbol{F}_{sv}$ that quickly drives the fluid to a configuration much closer to the equilibrium geometry; whereupon the local volume force $\boldsymbol{F}_{sv}$ becomes much smaller. This treatment of wall adhesion is found to give the correct sign for the wall adhesion force, but can underestimate its magnitude, especially in the wall cells having a large fractional area blocked to flow.

Example Calculations

RIPPLE has been applied to a wide variety of low-speed flow problems, some of which have been reported in the literature.[1,2] Two examples illustrating RIPPLE's capabilities are discussed in the following.

Jet-Induced Tank Mixing

A number of fluid flow scenarios in a reduced gravity environment call for the use of a jet, e.g., to fill tanks to capacity or to induce mixing of fluid in partially filled tanks. For example, cryogenic propellant tanks are vulnerable to heat additions that lead to excessive thermal stratification, and hence to undesirable rates of pressure increase. The jet enhances thermal transport by inducing mixing, insuring a more uniform fluid temperature. Jets might also be used in no-vent fill processes, in which a tank is filled to capacity without venting the remaining vapor.[16] The residual vapor must be condensed during the fill process to make room for incoming liquid. An important jet design component that can be addressed with RIPPLE is the optimal velocity of the jet, which depends on the application. For example, an optimal jet velocity might be one that maximizes liquid recirculation without penetrating or disrupting the free surface, which could destroy the mixing process. On the other hand, penetration of the free surface might be desired, which allows the jet to impinge on the opposite tank walls and promote vapor condensation as an aid to the no-vent fill process.

As an example of low-gravity tank flows induced by an internal jet, a half-full liquid hydrogen (LH_2) propellant tank (radius 210 cm, height 1020 cm), representing a typical orbital transfer vehicle conceptual design, was chosen. An internal jet (radius 10 cm, height 60 cm) is centered on the cylindrical axis at the bottom of the tank. The jet velocity is set at 4 cm/s, corresponding to a Weber number ($We = \rho R V^2/\sigma$, where R is the jet radius) of approximately 6. The LH_2, prior to turning on the jet, is initially in an equilibrium meniscus position with $\theta_{eq} = 5$ deg as the equilibrium contact angle.

The jet-induced tank flow is coarsely resolved with a nonuniform 14×34 mesh that is refined along the tank axis of symmetry and wall. The fluid is given the properties of inviscid LH_2 in cgs units, and is initially upright in an equilibrium meniscus position. Gravity is zero. Accurate time resolution over this flow period follows from limiting the time step to a

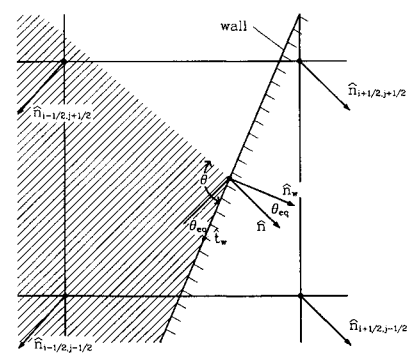

Fig. 3 RIPPLE treatment of the wall adhesion boundary condition on a right wall. The boundary condition is applied at two rightmost vertex normals, and since the free surface makes an angle $\theta \neq \theta_{eq}$ at the wall, a nonzero wall adhesion force results that tends to pull the fluid into a $\theta = \theta_{eq}$ configuration.

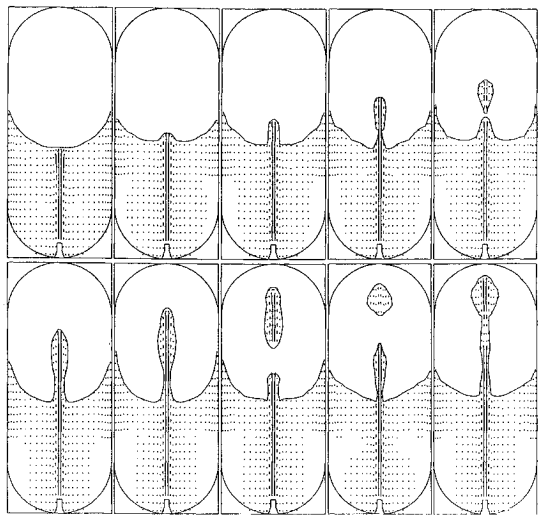

Fig. 4 Fluid velocity vectors and free-surface configurations at times of (left-to-right, top-to-bottom) 200, 600, 1200, 1400, 1600, 2000, 2200, 2400, 2600, and 3000 s for the jet-induced tank flow problem. The velocity of fluid exiting the jet at the tank bottom is 4 cm/s.

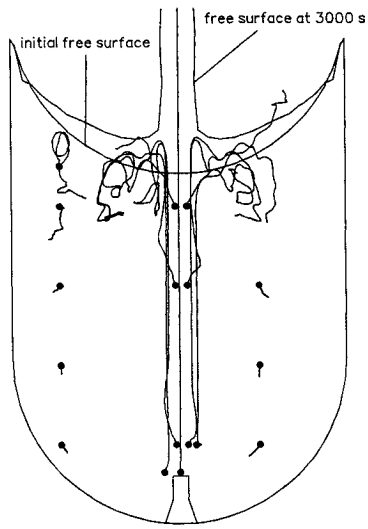

Fig. 5 Trajectories of Lagrangian marker particles initially located at various positions (denoted by dots) in the tank flow displayed in Fig. 4.

value of 2.0 s. The obstacle enclosing the jet is characterized with small modifications to the RIPPLE source code.

For a jet velocity of 3 cm/s ($We \sim 3.5$), RIPPLE calculations indicate that surface tension forces are just able to hold back the laminar jet. As shown in Fig. 4, the case is different for a laminar jet of 4 cm/s ($We \sim 6$). Blobs of fluid are detached from an intense central geyser of fluid. At times later than 3000 s (where Fig. 4 ends), blobs are thrown against the top of the tank. The first blob wets the tank fairly evenly, while the second accumulates around the jet impingement region.

A new feature in RIPPLE is the capability to track fluid properties sampled by Lagrangian marker particles. This permits a more detailed analysis of complex flowfields. Some marker trajectories are displayed in Fig. 5 for the jet-induced tank flow. The most intricate motions are displayed by particles near the tank centerline. For these particles, the initial motion during entrainment may be directed either toward or away from the jet. There follows an entrained motion terminating near the free surface, whereupon the particle motions become very chaotic, reflecting the complex pattern of surface waves generated by the jet. Particles near the tank walls have shorter and less intricate trajectories, except for particles near the fluid surface. The Lagrangian particles are an important diagnostic in this calculation, showing two features of the flow that are not otherwise readily apparent: 1) tank fluid far from the centerline is not entrained by the laminar jet, and 2) tank fluid near the jet opening comprises the leading portion of the first blob that is ejected from the main fluid body.

Jet-induced flows are excellent examples of fluid flows that can be modeled more realistically when turbulent effects are included. The jet in these calculations would tend to diffuse radially, dissipating a portion of its kinetic energy into turbulent energy, with the addition of a turbulence model such as the k-ϵ model.[17] The turbulent jet velocities required to geyser the free surface would likely be higher than the laminar jet velocities computed with the standard version RIPPLE. In lieu of a turbulence model, however, turbulent effects can be estimated with RIPPLE by using a turbulent eddy viscosity ν_t. One estimate for ν_t is $\nu_t \sim fsk^{1/2}$, where f is the fraction of jet kinetic energy dissipated into turbulence, s the turbulent length scale, and k the turbulent kinetic energy density. Reasonable values for the jet are $f = 0.10$; $s = R_j/2$, where R_j is the jet radius; and $k = fv_j^2/2$, where v_j is the jet velocity. With a 4.0 cm/s jet velocity, the addition of a turbulent eddy viscosity with these values dissipates the jet enough to prevent its penetration through the free surface.

Water Rod Collision

Consider the collision of two water drops, or infinite rods in two dimensions, impacting each other head-on at equal and opposite velocities. Although the phenomena of drop collision and coalescence is inherently three dimensional, a two-dimensional rod collision is interesting because it displays the competition between inertial and surface forces and exhibits the hydrodynamic phenomena of breakup and coalescence. Many

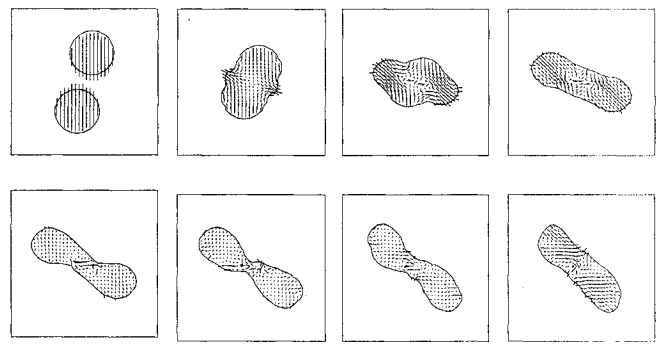

Fig. 6 Fluid velocity vectors and free-surface configurations at times of (left-to-right, top-to-bottom) 0.0, 0.1, 0.2, 0.3, 0.4, 0.5, 0.6, and 0.7 s for two rods of water, each with a radius of 1.5 cm, colliding at an equal and opposite velocity of 10 cm/s. The collision overlap is 1.33 radii.

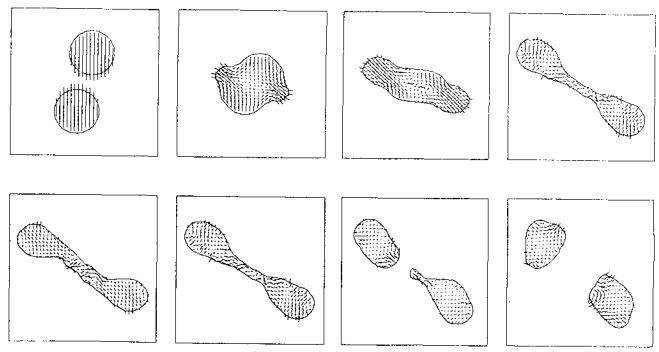

Fig. 7 Fluid velocity vectors and free-surface configurations at times of (left-to-right, top-to-bottom) 0.0, 0.1, 0.2, 0.3, 0.4, 0.5, 0.6, and 0.7 s for two rods of water, each with a radius of 1.5 cm, colliding at an equal and opposite velocity of 15 cm/s. The collision overlap is 1.33 radii.

computational models, such as boundary integral methods, cannot readily simulate such phenomena without special modifications. RIPPLE can, however, compute straight through pinch-off (see Fig. 7 and the example in Ref. 1) and coalescence (see Fig. 6).

A 10 cm × 10 cm computational domain, partitioned in planar geometry with a 40 × 40 mesh ($\delta x = \delta y = 0.25$ cm) is chosen to resolve the collision of two 1.5-cm radius rods that are given the properties of water, except for viscosity, which is neglected. The rods are initially given equal and opposite y velocities (one moving up and the other moving down). They collide head-on, overlapping by 1.33 radii. We wish to explore the competition between inertial and surface tension forces, which, in the end, determines whether the rods remain coalesced. Two different impact velocities are chosen for the rods: 10 cm/s ($We \sim 8.2$), shown in Fig. 6, and 15 cm/s ($We \sim 18.5$), shown in Fig. 7.

The two rods initially form a larger rod after impact that, because of the net angular momentum in the system, rotates in clockwise sense. Whether the larger rod maintains its integrity or breaks up depends on the relative magnitude of surface to inertial forces (i.e., the *We* number). It is evident from Fig. 6 that the inertial forces resulting from a 10 cm/s collision are not enough to overcome the surface tension forces. The bridge of water at $t = 0.5$ s is subject to sufficiently strong surface forces to prevent breakup. In Fig. 7, a collision velocity of 15 cm/s produces inertial forces sufficient to overcome surface forces, permitting the two rods to exchange momentum but retain their identity. The rods coalesce and then break up, pinching off at about 0.6 s. The lack of symmetry evident in Fig. 7 is the result of directional splitting in the VOF advection algorithm.

Status of RIPPLE

Like all numerical models, RIPPLE is continuing to evolve through algorithm enhancements, improvements, and additions, as driven by the needs of a growing user community. Models for heat and turbulence transport, variable surface tension effects, and multifluid flows are planned for the future. A three-dimensional version of RIPPLE is also planned. Algorithm improvements are also being incorporated into RIPPLE. An example is the Youngs VOF advection model[15] that allows the reconstructed free surface to have nonzero slope. Additional extensions of the RIPPLE methodology are pointed out in Sec. V of Ref. 1.

A detailed user manual[1] is available, and the RIPPLE source code can be obtained from the Energy Science and Technology Software Center [P.O. Box 1020, Oak Ridge, TN, 37831-1020, telephone (615) 576-2606].

Acknowledgments

This work was supported by the NASA Lewis Research Center, Interagency Agreement Order C-32008-K and the U.S. Department of Energy under Contract W-7405-ENG-36.

References

[1]Kothe, D. B., Mjolsness, R. C., and Torrey, M. D., "RIPPLE: A Computer Program for Incompressible Flows with Free Surfaces," Los Alamos National Lab., LA-12007-MS, Los Alamos, NM, April 1991.

[2]Brackbill, J. U., Kothe, D. B., and Zemach, C., "A Continuum Method for Modeling Surface Tension," *Journal of Computational Physics,* Vol. 100, No. 2, 1992, pp. 335–354.

[3]Kershaw, D. S., "The Incomplete Cholesky-Conjugate Gradient Method for the Iterative Solution of Systems of Linear Equations," *Journal of Computational Physics,* Vol. 26, No. 1, 1978, pp. 43–65.

[4]Addessio, F. L., Carroll, D. E., Dukowicz, J. K., Harlow, F. H., Johnson, J. N., Kashiwa, B. A., Maltrud, M. E., and Ruppel, H. M., "CAVEAT: A Computer Code for Fluid Dynamics Problems with Large Distortion and Internal Slip," Los Alamos National Lab., LA-10613-MS, Los Alamos, NM, Feb. 1986.

[5]Nichols, B. D., Hirt, C. W., and Hotchkiss, R. S., "SOLA-VOF: A Solution Algorithm for Transient Fluid Flow with Multiple Free Boundaries," Los Alamos National Lab., LA-8355, Los Alamos, NM, Aug. 1980.

[6]Torrey, M. D., Cloutman, L. D., Mjolsness, R. C., and Hirt, C. W., "NASA-VOF2D: A Computer Program for Incompressible Flows with Free Surfaces," Los Alamos National Lab., LA-10612-MS, Los Alamos, NM, Dec. 1985.

[7]Hotchkiss, R. S., "Simulation of Tank Draining Phenomena with the NASA SOLA-VOF Code," Los Alamos National Lab., LA-8163-MS, Los Alamos, NM, Dec. 1979.

[8]Hirt, C. W., and Nichols, B. D., "Volume of Fluid (VOF) Method for the Dynamics of Free Boundaries," *Journal of Computational Physics,* Vol. 39, No. 1, 1981, pp. 201–225.

[9]Hirt, C. W., Cook, J. L., and Butler, T. D., "A Lagrangian Method for Calculating the Dynamics of an Incompressible Fluid with Free Surface," *Journal of Computational Physics,* Vol. 5, No. 1, 1970, pp. 103–124.

[10]Harlow, F. H., and Welch, J. E., "Numerical Calculation of Time-Dependent Viscous Incompressible Flow of Fluid with Free Surface," *Physics of Fluids,* Vol. 8, No. 12, 1965, pp. 2182–2189.

[11]Daly, B. J., "A Technique for Including Surface Tension Effects in Hydrodynamic Calculations," *Journal of Computational Physics,* Vol. 4, No. 1, 1969, pp. 97–117.

[12]Floryan, J. M., and Rasmussen, H., "Numerical Methods for Viscous Flows with Moving Boundaries," *Applied Mechanics Review,* Vol. 42, No. 12, 1989, pp. 323–339.

[13]Landau, L. D., and Lifshitz, E. M., *Fluid Mechanics,* 1st ed., Pergamon, New York, 1959, pp. 230–234.

[14]Noh, W. H., and Woodward, P., "The SLIC (Simple Line Interface Calculation)," *Proceedings of the Fifth International Conference on Numerical Methods in Fluid Dynamics,* edited by A. I. van de Vooren and P. J. Zandbergen, Vol. 59, Lecture Notes in Physics, Springer-Verlag, New York, 1976, pp. 330–340.

[15]Youngs, D. L., "Time-Dependent Multi-Material Flow with Large Fluid Distortion," *Numerical Methods for Fluid Dynamics,* edited by K. W. Morton and M. J. Baines, Academic Press, New York, 1982, pp. 273–285.

[16]Aydelott, J. C., Gille, J. P., and Eberhardt, R. N., "On-Orbit Cryogenic Fluid Transfer," Twentieth Joint Propulsion Conference, AIAA Paper 84-1343, Cincinnati, OH, June 1984.

[17]Launder, B. E., and Spalding, D. B., *Mathematical Models of Turbulence,* Academic Press, New York, 1972, pp. 90–100.